

Improved kinetic analysis of dynamic PET data with optimized HYPR-LR

John M. Floberg^{a)}

Department of Medical Physics, University of Wisconsin-Madison, 1111 Highland Avenue, Madison, Wisconsin 53705

Charles A. Mistretta and Jamey P. Weichert

Department of Medical Physics, University of Wisconsin-Madison, 1111 Highland Avenue, Madison, Wisconsin 53705 and Department of Radiology, University of Wisconsin-Madison, 600 Highland Avenue, Madison, Wisconsin 53705

Lance T. Hall

Department of Radiology, University of Wisconsin-Madison, 600 Highland Avenue, Madison, Wisconsin 53705

James E. Holden and Bradley T. Christian

Department of Medical Physics, University of Wisconsin-Madison, 1111 Highland Avenue, Madison, Wisconsin 53705

(Received 10 December 2011; revised 1 May 2012; accepted for publication 2 May 2012; published 22 May 2012)

Purpose: Highly constrained backprojection-local reconstruction (HYPR-LR) has made a dramatic impact on magnetic resonance angiography (MRA) and shows promise for positron emission tomography (PET) because of the improvements in the signal-to-noise ratio (SNR) it provides dynamic images. For PET in particular, HYPR-LR could improve kinetic analysis methods that are sensitive to noise. In this work, the authors closely examine the performance of HYPR-LR in the context of kinetic analysis, they develop an implementation of the algorithm that can be tailored to specific PET imaging tasks to minimize bias and maximize improvement in variance, and they provide a framework for validating the use of HYPR-LR processing for a particular imaging task.

Methods: HYPR-LR can introduce errors into non sparse PET studies that might bias kinetic parameter estimates. An implementation of HYPR-LR is proposed that uses multiple temporally summed composite images that are formed based on the kinetics of the tracer being studied (HYPR-LR-MC). The effects of HYPR-LR-MC and of HYPR-LR using a full composite formed with all the frames in the study (HYPR-LR-FC) on the kinetic analysis of Pittsburgh compound-B ([¹¹C]-PIB) are studied. HYPR-LR processing is compared to spatial smoothing. HYPR-LR processing was evaluated using both simulated and human studies. Nondisplaceable binding potential (BP_{ND}) parametric images were generated from fifty noise realizations of the same numerical phantom and eight [¹¹C]-PIB positive human scans before and after HYPR-LR processing or smoothing using the reference region Logan graphical method and receptor parametric mapping (RPM2). The bias and coefficient of variation in the frontal and parietal cortex in the simulated parametric images were calculated to evaluate the absolute performance of HYPR-LR processing. Bias in the human data was evaluated by comparing parametric image BP_{ND} values averaged over large regions of interest (ROIs) to Logan estimates of the BP_{ND} from TACs averaged over the same ROIs. Variance was assessed qualitatively in the parametric images and semiquantitatively by studying the correlation between voxel BP_{ND} estimates from Logan analysis and RPM2.

Results: Both the simulated and human data show that HYPR-LR-FC overestimates BP_{ND} values in regions of high [¹¹C]-PIB uptake. HYPR-LR-MC virtually eliminates this bias. Both implementations of HYPR-LR reduce variance in the parametric images generated with both Logan analysis and RPM2, and HYPR-LR-FC provides a greater reduction in variance. This reduction in variance nearly eliminates the noise-dependent Logan bias. The variance reduction is greater for the Logan method, particularly for HYPR-LR-MC, and the variance in the resulting Logan images is comparable to that in the RPM2 images. HYPR-LR processing compares favorably with spatial smoothing, particularly when the data are analyzed with the Logan method, as it provides a reduction in variance with no loss of spatial resolution.

Conclusions: HYPR-LR processing shows significant potential for reducing variance in parametric images, and can eliminate the noise-dependent Logan bias. HYPR-LR-FC processing provides the greatest reduction in variance but introduces a positive bias into the BP_{ND} of high-uptake border regions. The proposed method for forming HYPR composite images, HYPR-LR-MC, eliminates this bias at the cost of less variance reduction. © 2012 American Association of Physicists in Medicine. [<http://dx.doi.org/10.1118/1.4718669>]

Key words: dynamic positron emission tomography, denoising, kinetic analysis, parametric images, [¹¹C]-PIB

I. INTRODUCTION

Highly constrained backProjection (HYPR) is a family of image reconstruction and post processing algorithms that have made a large impact on magnetic resonance angiography (MRA), allowing for undersampling factors on the order of several hundred fold and dramatic signal-to-noise ratio (SNR) improvements in dynamic datasets.^{1–3} The central idea of HYPR is to estimate individual frames in a dynamic study by weighting a temporally summed composite image. In the ideal case, individual frames will take on the noise properties of the composite image. It is the potential improvement in the SNR that makes HYPR an attractive tool for other imaging modalities, and we have recently applied the post-processing version, HYPR-LR (for local reconstruction), to positron emission tomography (PET) with promising results.⁴

One of the primary motivations for applying HYPR-LR to PET data is to improve the kinetic analysis methods used to analyze dynamic PET data, all of which are sensitive to noise to some degree. In our previous work, we demonstrated this with simple parameters estimated from phantom studies (e.g., nonlinear least squares fitting to estimate radionuclide decay constants).⁴ In these studies, we summed all the frames of the study to form the composite image, as this will provide the greatest enhancement in the SNR. However, it is well understood that differences between the composite image and the frame of interest can distort the temporal signals of neighboring regions with different temporal behaviors.¹ In the context of quantitative kinetic analysis, the bias caused by HYPR-LR processing may have an impact on the analysis, which should be accounted for and controlled as best as possible. Traditionally, bias in HYPR processing has been minimized by using a sliding composite window, so that composite images are more similar to their corresponding frames.¹ While such an approach may potentially be effective for dynamic PET data, it is arbitrary, and the optimal implementation of HYPR-LR will be dependent on the specific imaging task. In addition, as the noise reduction provided by HYPR-LR will be dependent on the number of counts in the composite (i.e., its temporal duration) relative to the frame of interest,^{1,2} it will provide the greatest benefit when the composites are made using as long an integration time as possible without introducing any bias. If composite images are shorter than this, they will provide no increased benefit in terms of reduced bias, and if they are made larger than this the additional noise improvements gained will come at the cost of bias.

In this work, we aim to develop an optimized implementation of HYPR-LR that can be tailored to individual PET studies such that it will provide the greatest reduction in variance while minimizing bias introduced by the algorithm, and to closely evaluate the performance of HYPR-LR processing in the context of quantitative kinetic analysis. We attempt to fulfill these aims using a combination of simulated and real human data of a tracer of interest to us, [¹¹C]-Pittsburgh compound-B (PIB). [¹¹C]-PIB is amenable to analysis using a number of techniques, including Logan graphical analysis,⁵

a data driven method with a well-known noise-dependent bias,^{6–8} and simplified reference tissue model (SRTM) methods,⁹ which are model based and not sensitive to bias.^{10–12} The basis function implementation of SRTM, so called receptor parametric mapping (RPM or RPM2), is regarded as more robust than the Logan method with respect to both variance and bias.⁹ We examine the effects of our proposed implementation of HYPR-LR processing on both the bias and precision of nondisplaceable binding potential (BP_{ND}) estimates obtained with both Logan graphical analysis and RPM2. We do this in the context of parametric image generation, as single voxel analysis will be the most sensitive to noise. Simulated data are used to illustrate the trade-off between bias and variance in absolute terms where the truth is known, and human data are used to illustrate the algorithm's properties in the context of a real imaging task. While, we focus on two analysis methods for [¹¹C]-PIB data here, we also intend to provide a framework for determining the optimal implementation of HYPR-LR for a given imaging task that can be generalized to other tracers and analysis methods.

II. THEORY

All of the formulations of HYPR make use of a temporally summed composite image in a dynamic set of images to provide a low-noise estimate of the true image at an individual time frame. This composite is weighted by a low resolution spatial comparison of each frame and the composite image. In the case of HYPR-LR, the spatial comparison is achieved by convolving the frame of interest and the composite image with a filtering kernel

$$H_t = C_t \cdot W_t = C_t \cdot \frac{I_t \otimes F}{C_t \otimes F}, \quad (1)$$

where H_t is the HYPR-LR estimate of an individual frame at time t , C_t is the composite image used for time t , W_t is the weighting image, I_t is an initial reconstruction of the frame, F is the filtering kernel, and \otimes represents the convolution operation. When images are sparse, as they are in angiography, so long as two objects with different temporal behaviors do not overlap in the filtering process, they will be perfectly reproduced.² Unfortunately, in non sparse images, such as those in PET, regions with different temporal behavior will invariably overlap in the filtering process, potentially creating a bias. This bias will manifest itself at high-frequency boundaries since the weighting image is formed by a low-frequency comparison.

The only way for the HYPR-LR estimate of a PET frame to be perfectly accurate is if the contrast between objects present in an individual frame is the same as the contrast between those objects in the frame's composite image. Failing this, errors at high-frequency boundaries will depend on the difference in contrast between neighboring regions and the size of the kernel used (Fig. 1).

Quantitatively accurate application of HYPR-LR to PET data may still be possible because of the predictable behavior of PET tracers. This predictable behavior can be used to form composite images that more closely fulfill our criteria of

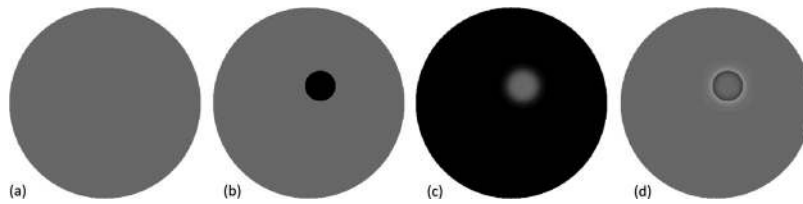


FIG. 1. Illustration of the errors HYPR-LR can cause. The original image in this case is uniform (a), but a region of high uptake is revealed in the composite image (b). As a result, the weighting image (c) is inappropriately blurred, creating errors in the HYPR-LR result (d).

having the same contrast between objects as their corresponding frames, and our proposed optimized implementation of HYPR-LR for PET data attempts to achieve this. We divide a typical tracer's behavior into three phases: uptake, specific retention, and equilibrium. Immediately after a tracer's injection, during the brief uptake phase, the activity in all regions will be increasing at a relatively constant rate. As a tracer is retained in regions of specific avidity, these regions begin to distinguish themselves from the background in a predictable manner. Finally, the tracer will reach a time of equilibrium, known as t^* , the attainment of which is required for application of graphical analysis methods and after which the image changes very little.^{6,7,13,14} Figure 2(a) illustrates these behaviors for [^{11}C]-PIB for different regions of the brain. A composite image could thus be formed for the uptake and equilibrium phases by summing all the frames in these phases. A sliding composite could be used during the retention phase such that the change in contrast is nearly linear for the frames used, creating a composite very similar to the individual frame being processed.

The formation of the composite images can thus be described as:

$$\text{For } t = 1 \text{ to } t_{\text{uptake}} \quad C_t = \sum_{t'=1}^{t_{\text{uptake}}} I_{t'} \cdot \Delta_{t'}, \quad (2a)$$

$$\text{For } t = t_{\text{uptake}} + 1 \text{ to } t^* - 1 \quad C_t = \sum_{t'=t-\alpha}^{t+a} I_{t'} \cdot \Delta_{t'}, \quad (2b)$$

$$\text{For } t = t^* \text{ to } t_{\text{max}} \quad C_t = \sum_{t'=t^*}^{t_{\text{max}}} I_{t'} \cdot \Delta_{t'}. \quad (2c)$$

Note that t denotes frame, not time. The phases of the study are demarcated here by t_{uptake} , the frame at which the uptake phase ends, t^* , the frame at which the steady state begins, and t_{max} , the final frame of the study. The parameter α determines the number of frames to be used in the sliding composite during the specific retention phase, and Δ_t is the duration of frame t . It is also important to note that data should not be decay corrected, so that each frame is weighted based on counts in its contribution to the composite image. Decay correction is applied after HYPR-LR processing.

The temporal parameters in Eq. (2) must be determined from the data to be analyzed. We propose doing this on a region of interest (ROI) level. Specifically, ROIs should be drawn over structures in the image, and the ratios of neighboring structures must be examined. More emphasis can be put on structures of relevance. We illustrate this here with the parietal cortex and its surrounding structures in the case of a real [^{11}C]-PIB dataset [Fig. 2(b)]. The parameters t_{uptake} and t^* can be determined by identifying the end of the flat

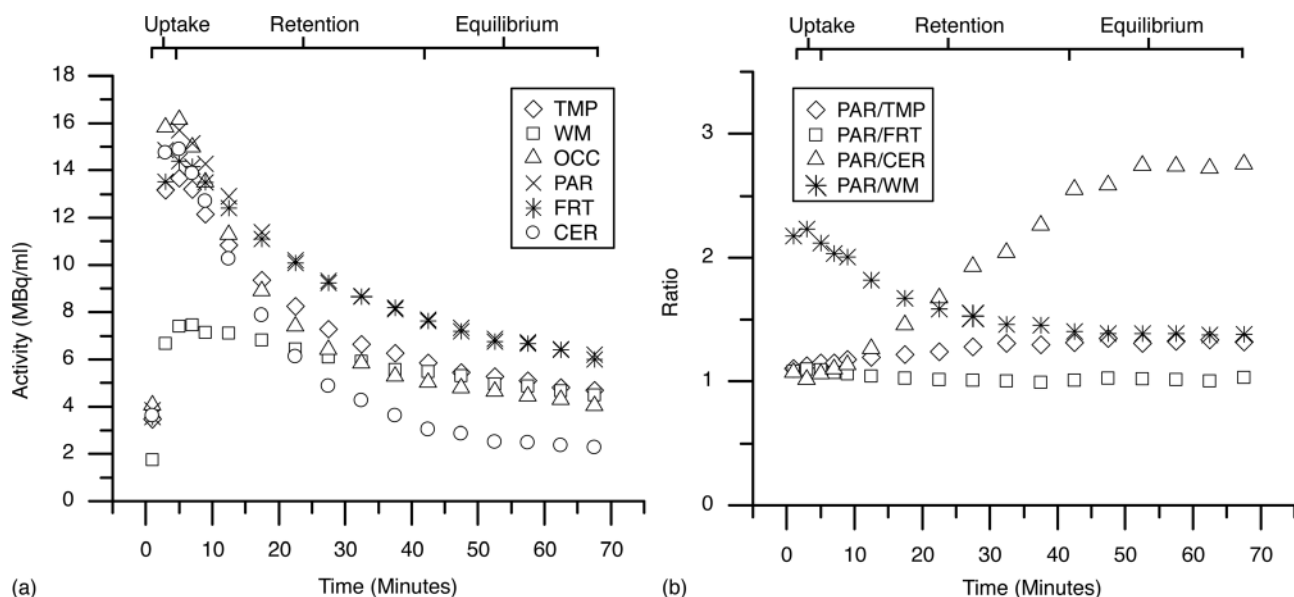


FIG. 2. [^{11}C]-PIB TACs for regions of the brain from a [^{11}C]-PIB positive human study (a), and the ratio of the activities of neighboring regions at each time point (b). The phases of the tracer's temporal behavior can be used to form more appropriate temporally dependent composite images for HYPR-LR. (PAR = parietal cortex, FRT = frontal cortex, TMP = temporal cortex, OCC = occipital cortex, WM = white matter, and CER = cerebellum).

uptake phase and the start of the flat equilibrium phase, respectively. α is more arbitrary, and we propose selecting a value such that the composite image is 10–20 min (5–7 frames) in duration for a typical PET imaging study. The frames at the beginning and end of the retention phase will largely determine the size of α , and α should be made as large as possible while keeping the contrast in the composite images for these frames as close as possible to the contrast in the frames themselves. This process could be performed for individual patients, or for a general population for whom a tracer's temporal behavior is relatively consistent.

The size of the kernel, F , used in the formation of the weighting image is the other parameter which must be determined. The size of the kernel will determine the degree to which regions with disparate temporal behaviors overlap and contribute to bias, and also determine the spatial frequencies of individual frames that effectively take on the noise properties of their composite images. If our composite scheme is implemented correctly and the contrast between objects in individual frames and their respective composites is nearly the same, overlap between regions should contribute little to temporal errors. A larger kernel should thus be desirable, as it will suppress noise at a wide range of spatial frequencies. In this work, the largest kernel used was a 3D Gaussian with a FWHM approximately double the resolution of the scanner, 9 mm in this case. If the composite images do not match their respective frames, a relatively small kernel should be used to limit bias. The smallest kernel use in this work was a 3D Gaussian with a FWHM of 3 mm, close to the thickness of the cortex, the primary object of interest for [^{11}C]-PIB. We evaluate the effects of different kernel sizes as outlined in our methods.

Our proposed method of forming multiple composite images will itself be limited in a number of respects. For one, it will likely not be possible to perfectly fulfill our criterion of forming composite images having the same contrast between objects as in their respective frames. However, so long as there is not substantial bias introduced into multiple frames, having a few frames slightly biased by imperfect composite images should not affect kinetic analysis a great deal. Second, not all dynamic PET studies will be amenable to our particular method of forming composites described in Eq. (2), for example tracers with a washout phase. Finally, using shorter composite images will increase the variance in individual frames and parametric images. Nevertheless, the ratio of the activities of neighboring regions should at least be examined to provide insight into what time-series data will produce composite images those objects in the respective frames. We believe this will allow for the maximum benefit in terms of variance reduction while minimizing bias for a given PET tracer and imaging task.

III. METHODS

III.A. Creation of numerical phantoms

As HYPR-LR uses data in both space and time to provide an estimate of each voxel value in time-series PET data, a realistic spatial distribution of time activity curves (TACs) must be used for simulated data. The spatial and temporal

distribution of added noise must also reasonably represent what would be expected in a PET acquisition. We created spatial distributions of TACs using the Zubal brain phantom,¹⁵ and TACs from a human [^{11}C]-PIB acquisition. The [^{11}C]-PIB TACs used were taken from a [^{11}C]-PIB positive human scan acquired at our center over 70 min with 5×2 and 12×5 min frames. ROIs were drawn over the frontal cortex, parietal cortex, occipital cortex, temporal cortex, white matter, and cerebellum on a temporally summed image (Fig. 2). The resulting temporal patterns were used to create a noise-free dynamic image set by impressing the TAC values into their corresponding regions in the Zubal phantom image.

A PET acquisition on an ECAT HR+ scanner was then approximated using published performance information about the scanner model.^{16,17} Data were first resampled to voxel sizes of $2.2 \times 2.2 \times 2.45$ mm, and then smoothed with a $4.39 \times 4.39 \times 5.10$ mm³ full-width-at-half-maximum (FWHM) Gaussian to approximate the resolution of the scanner. The activity distributions in the smoothed noise-free phantoms were converted into expected counts by multiplying by factors for decay correction, frame duration, and voxel volume. Data in each slice were then forward projected at 160 angles spaced at 1.125° using MATLAB's (The MathWorks®) two-dimensional radon transform function (i.e., a two-dimensional acquisition). An attenuation map for each slice was created by assigning all voxels identified as bone in the Zubal brain phantom an attenuation coefficient of bone, and all voxels identified as other tissues an attenuation coefficient of water at 511 keV. The attenuation map was then resampled to the same matrix size as the PET images, thus creating some voxels with intermediate attenuation coefficients, and forward projected at the same angles as the emission data. Each simulated emission sinogram was multiplied by its corresponding attenuation sinogram and the published sensitivity of the scanner. Scatter was not modeled, but the sinograms were multiplied by the expected scatter fraction for the amount of activity used in the simulation. While this does not accurately model scatter, it will reduce the counts in the simulated sinograms to a similar degree as a true scatter correction algorithm so that the added count-dependent Poisson noise is appropriately scaled. A noisy data value was then given to each position in the resulting sinograms by generating a random number from a Poisson distribution with a mean equal the value of that position in the noise-free sinograms. The resulting noisy sinograms were reconstructed with filtered backprojection (FBP) using a ramp filter with a cut-off at 0.75 the Nyquist frequency after correcting for attenuation, and values in the resulting images were converted back to activity units (Bq/ml). Fifty noisy realizations of the same simulated [^{11}C]-PIB dataset were produced in this way. The noise-free sinograms were also reconstructed with FBP to generate a standard to compare the HYPR-LR processed data to. FBP reconstruction was used as it is an analytical method that does not introduce any bias of its own, unlike iterative reconstructions like expectation-maximization (EM) and maximum *a posteriori* (MAP). This will allow for a more thorough evaluation of

the bias and variance properties of HYPR-LR that is not confounded by the tradeoff between bias and variance in the reconstruction itself.

III.B. Acquisition of real data

Eight human [^{11}C]-PIB datasets were evaluated to illustrate the potential of HYPR-LR to improve the kinetic analysis of real data. These datasets were selected as a representation of [^{11}C]-PIB positive scans from approximately 150 human studies performed at our institution to date. All data were obtained in accordance with our human subjects' research protocol approved by our institutional review board. Briefly, the PET data were acquired using a Siemens HR+ scanner in 3D mode (septa retracted). A 5 min transmission scan was first acquired for attenuation correction, followed by a 70 min dynamic emission scan initiated with a 30 s bolus infusion of radiotracer (518–585 MBq). The data were divided into 5×2 min frames and 12×5 min frames and reconstructed using a filtered back-projection algorithm using a ramp filter to a voxel size of $2.0 \times 2.0 \times 4.25 \text{ mm}^3$ and corrected for random events, attenuation of annihilation radiation, dead-time, scanner normalization, and scatter radiation.

III.C. HYPR-LR processing and smoothing

Both the real data and the simulated data were processed with HYPR-LR using either a full composite formed from all the data in the study (HYPR-LR-FC), or our proposed method of forming multiple composites (HYPR-LR-MC). The relevant temporal parameters for Eq. (2) were determined in the same manner demonstrated in Fig. 2. After examining the ratios of the activities of neighboring regions in both the simulated data and all the human datasets, we determined that the same temporal parameters could be used for all the data. Namely, t_{uptake} was set at frame 3 (6 min), α was set to 2 frames (5 frames total in the sliding window), and t^* was set at frame 12 (40 min). To study the impact of kernel size, we used three-dimensional Gaussian filtering kernels with a FWHM in each spatial dimension of three different sizes: 3, 6, and 9 mm. The $9 \times 9 \times 9 \text{ mm}^3$ FWHM kernel was used to process all of the human data to examine both the maximum improvement in variance and the maximum bias to be expected from HYPR-LR processing. It is important to note that some protection against small numbers in the denominator of Eq. (1) must be implemented. We do this by setting all voxels in the blurred composite image

whose values fall below 1% of the maximum of the unblurred composite image to zero. All voxels in the weighting image whose value includes a division by zero are also set to zero. Table I summarizes HYPR-LR terminology used frequently in this work.

Simulated and real data were also smoothed (after reconstruction) to provide a simple denoising method to compare HYPR-LR processing to. Both real and simulated data were smoothed with $3 \times 3 \times 3$ and $6 \times 6 \times 6 \text{ mm}^3$ FWHM Gaussian kernels. Although not as sophisticated as other denoising techniques, smoothing either within or after the reconstruction process is still one of the most widely used denoising methods. And while the improvement in noise obtained with HYPR-LR processing comes from the composite image,² we refrain from comparing HYPR-LR to simple filtering in the time domain as this will distort TACs by introducing temporal correlations. HYPR-LR processing does have the potential to distort TACs, but one of the explicitly stated aims of this work is to determine how to minimize such distortions.

III.D. Kinetic analysis

Parametric images of both the simulated and human data were created using the data driven reference region Logan graphical method and the model based RPM2 method. Logan graphical analysis is relatively easy to implement, assumes no particular model, and can provide reliable and robust BP_{ND} estimates when data are noise-free.⁷ However, when the data are noisy, as they are when single voxel analysis is performed, Logan estimates of BP_{ND} are beset by bias and variance.⁸ RPM2 is regarded as having more favorable properties than the Logan method with regards to both bias and variance,^{11,12} and although it assumes a single tissue compartment model, it has proven to be an effective method for generating parametric images of [^{11}C]-PIB studies.⁹ We focus on parametric images as single voxel analysis will be very sensitive to noise and loss of resolution. HYPR-LR processing could thus be of great benefit to parametric imaging as it improves noise without sacrificing spatial resolution. HYPR-LR denoising could also improve ROI analysis, but the benefits of the algorithm will diminish as ROI size increases and the effects of noise decrease.

III.D.1. Logan graphical analysis

Simulated and human data were evaluated with the reference tissue Logan graphical method,⁷ using the cerebellum

TABLE I. A summary of HYPR-LR terminology.

Term	Definition
HYPR-LR	Highly constrained backProjection-Local Reconstruction
Composite image	Temporally summed (i.e., time-averaged) image used in the estimation of individual frames in HYPR-LR processing
Weighting image	Spatial comparison of an individual frame with its composite image used to weight the composite image
F , Filtering kernel	The smoothing kernel used to make the spatial comparison between an individual frame and its composite image
HYPR-LR-MC	HYPR-LR with multiple composite images
HYPR-LR-FC	HYPR-LR with a full composite image (summed over all frames)

as a reference region. For all [^{11}C]-PIB data, a reference tissue efflux constant, $k_{2\text{REF}}$, of 0.144 min^{-1} was used,^{5,18} and the equilibrium time, t^* , was determined from the data and set at 40 min. The distribution volume ratios (DVRs) generated at each voxel were converted to BP_{ND} values ($\text{BP}_{\text{ND}} = \text{DVR} - 1$) to give a parametric image of the non-displaceable binding potential. For the simulated data, the parametric image generated from the noise-free FBP reconstruction was used as a standard parametric image to which all parametric images generated from the noisy simulated data were compared. The reference region Logan method is data driven and assumes no model, and therefore should be the least biased of any reference tissue method when there is no noise in the data.

III.D.2. Receptor parametric mapping (RPM2)

Parametric images of the simulated and real datasets were also generated using the basis function implementation of SRTM using a fixed $k_{2\text{REF}}$ (RPM2).^{11,12} This method assumes that all TACs in the data can be fit to the simplified reference tissue model using following equation:

$$C_{\text{TAC}}(t) = R_1 C_{\text{REF}}(t) + R_1 (k_{2\text{REF}} - k_2) \times C_{\text{REF}}(t) \otimes \exp(-k_2 t) \quad (3a)$$

$$R_1 = \frac{K_1}{K'_1} \quad (3b)$$

$$\text{BP}_{\text{ND}} = R_1 \frac{k_{2\text{REF}}}{k_2} - 1 \quad (3c)$$

where $C_{\text{TAC}}(t)$ is the TAC, $C_{\text{REF}}(t)$ is the reference tissue TAC, K_1 and K'_1 are the influx rate constants for the TAC and the reference tissue, respectively, and k_2 and $k_{2\text{REF}}$ are the efflux rate constants for the TAC and the reference tissue, respectively. RPM2 creates a set of exponential basis functions over a range of k_2 values to simplify the fitting process. For the [^{11}C]-PIB data, we used a $k_{2\text{min}}$ of 0.02 min^{-1} and a $k_{2\text{max}}$ of 0.1 min^{-1} , with 50 basis functions. These minimum and maximum values for k_2 were derived from nonlinear least squares fits to Eq. (3) of several ROI TACs from both real and simulated data. Our minimum k_2 value falls slightly above the value obtained from non-linear least squares fits to some of the data, but gives results that are most consistent when compared with the Logan results. After an initial fitting of each voxel in the image using Eq. (3), $k_{2\text{REF}}$ is fixed to the median $k_{2\text{REF}}$ value of all voxels with a $\text{BP}_{\text{ND}} > 0$ and a second fitting is performed. We concerned ourselves only with the BP_{ND} parametric images generated by RPM2.

RPM2 requires that each frame be weighted by its duration and the total number of counts in the frame (without decay correction):¹¹

$$\text{Frame Weight} = \frac{(\text{Frame duration})^2}{\text{Total counts in frame}} \quad (4)$$

The unprocessed data were weighted in this fashion, but a different weighting scheme is required for the HYPR-LR processed data, as the variance in each frame will no longer be determined by the number of counts in the frame, but by the number of counts in the composite image. The frames in the HYPR-LR processed data were therefore weighted as (again, without decay correction):

$$\text{HYPR-LR Frame Weight} = \frac{(\text{Composite duration})^2}{\text{Total counts in composite}} \quad (5)$$

Fits to the HYPR-LR-FC data will thus be uniformly weighted as the same composite is used for each frame.

III.E. Data evaluation

III.E.1. Bias and variance in the simulated data

We studied the impact of HYPR-LR processing on kinetic analysis methods in absolute terms by evaluating the bias and variance of the parametric images generated from the simulated data. The bias at each voxel in the parametric images was taken as the percentage difference between the mean voxel values over the 50 noise realizations and the voxel values in the reference Logan parametric image generated from the noise-free FBP reconstruction. Bias in the parametric image voxels can be described as:

$$\text{bias}(\%) = \frac{\mu_x - x}{x} \cdot 100 \quad (6)$$

where μ_x is the mean voxel value over all noise realizations and x is the true voxel value.

The variance in the data were evaluated using the coefficient of variation (COV) at each voxel:

$$\text{COV} = \frac{\sigma_x}{\mu_x} \quad (7)$$

where σ_x is the standard deviation of a voxel over all noise realizations. The mean bias and COV of all voxels in the parietal and frontal cortices is reported (11 794 voxels).

III.E.2. Evaluation of human data

A ROI based kinetic analysis was used to evaluate bias in the parametric images of the human data. For each dataset, ROIs were drawn over the frontal and parietal cortex (regions of particular interest in [^{11}C]-PIB scans) on temporally summed images. ROIs contained 2648 voxels on average (range 1150–4385 voxels). The TACs from these ROIs were analyzed with the reference Logan graphical method with the same parameters described above to generate an average BP_{ND} value for the entire corresponding region. Over such a large region, the Logan estimates of the BP_{ND} should be relatively unbiased as there is little noise in the TAC and a single tissue compartment model is not assumed. These BP_{ND} values were thus used as a standard and compared with the BP_{ND} values from the same regions in the parametric images. In the ideal case, the BP_{ND} values taken from the parametric

images will match the ROI Logan estimates exactly. A bias will appear as a deviation from unity in the slope of a linear fit to the data, or a deviation from zero in the y-intercept.

The values of individual voxels in the parietal and frontal cortex of the parametric images generated with the reference Logan method and RPM2 were also compared before and after processing to give an indication of variance in the images. For each human [^{11}C]-PIB dataset, the voxel values obtained with each method were plotted against each other and fit to a straight line. The Pearson correlation coefficient (r) of the resulting fits should provide an indication of the variance in the parametric images. The use of correlation between the results of two analysis methods to indicate variance assumes that the effect of noise in the time-series data on the BP_{ND} estimates is independent for Logan analysis and RPM2. This approach therefore only gives a semiquantitative estimate of the variance in the parametric images. The correlation coefficients obtained from each dataset were compared between the original data, smoothing with a $3 \times 3 \times 3 \text{ mm}^3$ FWHM Gaussian, HYPR-LR-MC, and HYPR-LR-FC using paired t-tests.

IV. RESULTS

IV.A. Evaluation bias and variance in the simulated data

The simulated data were used as a means for illustrating the potential bias that HYPR-LR can introduce, and to precisely define the tradeoff between bias and variance when using the HYPR-LR algorithm in the context of quantitative

kinetic analysis for parametric image generation. The noise-free simulated data give insight into the bias that can be introduced into TACs, and hence quantitative kinetic parameters, by HYPR-LR processing. In the case of the simulated [^{11}C]-PIB data studied here, HYPR-LR-FC processing increases the BP_{ND} in regions of high uptake and decreases BP_{ND} in neighboring voxels with lower uptake, whereas the proposed method of multiple composite images (HYPR-LR-MC) introduces no obvious bias. This is seen in parametric images generated from the noise-free data with both the reference region Logan method and RPM2 [Figs. 3(a)–3(f)]. The bias caused by HYPR-LR-FC is due to distortions in the TACs, which are eliminated with HYPR-LR-MC [Fig. 3(g)]. It is also interesting to note that RPM2 globally increases BP_{ND} values, particularly in the white matter. This may be due to the inappropriateness of the simplified reference tissue model for the white matter.

Both HYPR-LR-MC and HYPR-LR-FC substantially improve the bias and variance of the Logan parametric images generated from the noisy simulated data. Greater reduction in both the noise-dependent Logan bias and the coefficient of variation of the binding potentials is achieved with larger filtering kernels [Fig. 4(a)]. For example, HYPR-LR-MC with a $9 \times 9 \times 9 \text{ mm}^3$ FWHM Gaussian kernel reduces the mean bias in the frontal and parietal cortex from -37.1% to -0.21% and the average COV from 33.1% to 11.0% . HYPR-LR-FC with the same kernel further reduces the COV to 6.37% and introduces a slight positive bias of 2.45% . This positive bias is consistent with what is observed in Fig. 3. The parametric Logan images generated from the

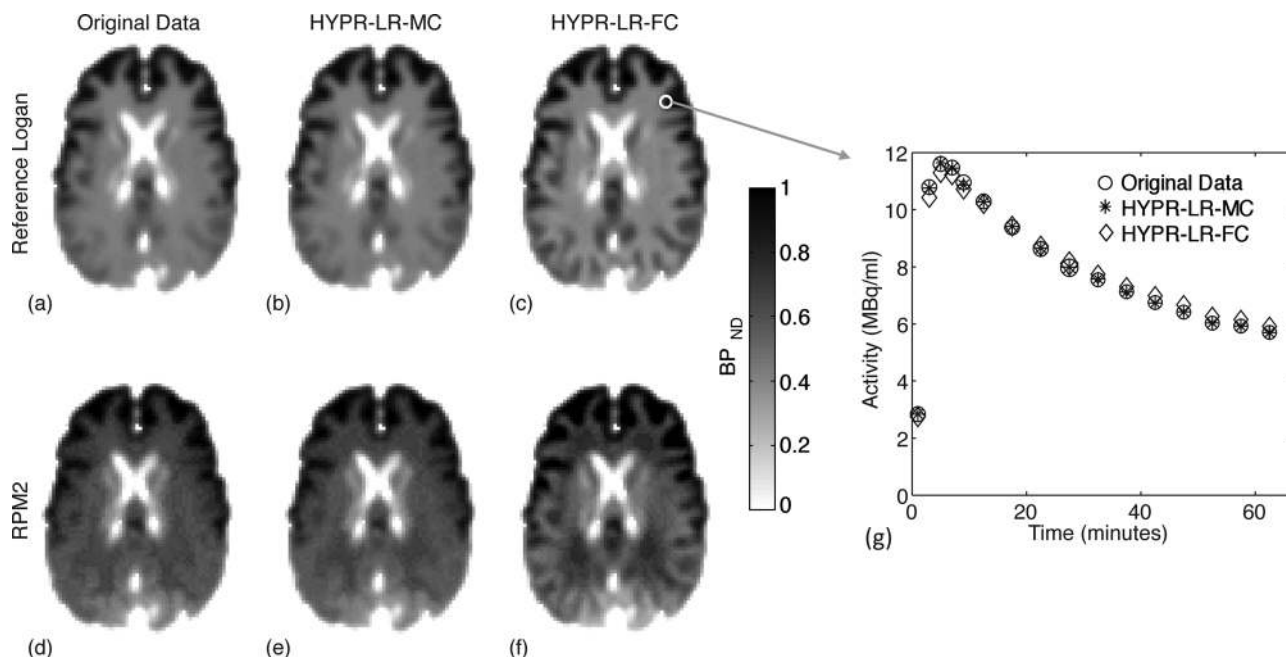


FIG. 3. Parametric images generated from the noise-free simulated data with either the reference region Logan graphical method (a)–(c) or RPM2 (d)–(f). RPM2 tends to overestimate BP_{ND} values in some regions, particularly the white matter. The parametric images generated from the data processed with the proposed method of forming composite images, HYPR-LR-MC (b) and (e), differ little from the parametric images generated from the unprocessed data (a) and (d). The parametric images generated from the data processed using HYPR-LR-FC (c) and (f) show greater contrast between the high uptake regions of cortex and the surrounding white matter. The biased BP_{ND} values seen with HYPR-LR-FC are due to changes in the TACs, demonstrated here for a small ROI (g). HYPR-LR-MC eliminates the bias in the TACs.

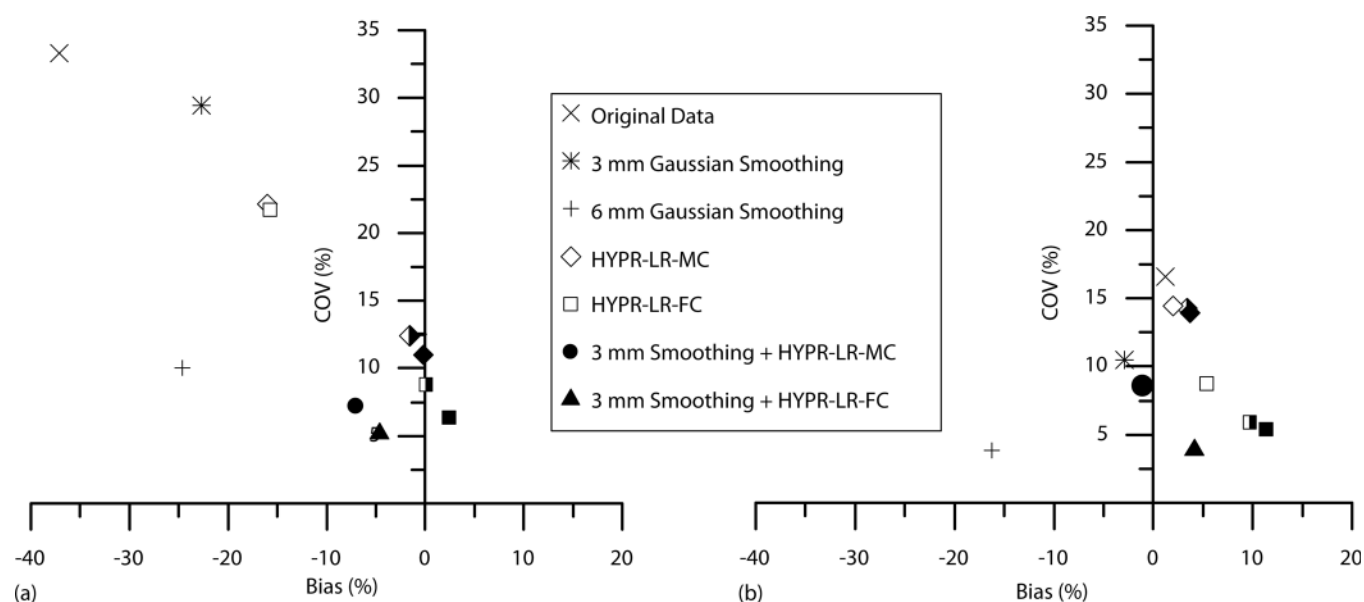


FIG. 4. The relationship between bias and variance for the BP_{ND} parametric images generated from the noisy simulated data with the reference region Logan graphical method (a) and RPM2 (b). The mean bias and coefficient of variation of voxels in the frontal and parietal cortices are shown for the parametric images generated from the original data, the data smoothed spatially with $3 \times 3 \times 3$ and $6 \times 6 \times 6$ mm³ FWHM Gaussians, and for the data processed with HYPR-LR-MC and HYPR-LR-FC using smoothing kernels with either a 3 mm FWHM (open shapes), a 6 mm FWHM (half-open shapes), or a 9 mm FWHM Gaussian (solid shapes). The mean bias and coefficient of variation following both spatial smoothing with a 3 mm FWHM Gaussian and HYPR-LR-MC and HYPR-LR-FC processing with a 9 mm FWHM Gaussian kernel are also shown.

HYPR-LR processed data compare very favorably with the images generated from the data that were smoothed with Gaussian filtering kernels. The $3 \times 3 \times 3$ mm³ FWHM Gaussian smoothing reduces the average bias to -22.7% and the average COV to 29.5% , and the $6 \times 6 \times 6$ mm³ FWHM Gaussian smoothing reduces the average bias to -24.6% , and the average COV to 10.0% . The bias in the data smoothed with the $6 \times 6 \times 6$ mm³ kernel is due mostly to the substantial blurring of the data.

HYPR-LR-MC and HYPR-LR-FC processing also reduce the variance in the parametric images generated with RPM2. The variance reduction provided by HYPR-LR-MC processing is not as great as in the Logan images, but it does provide an improvement while introducing little bias. Variance reduction increases as larger kernels are used and little additional bias is introduced [Fig. 4(b)]. For example, the average COV is reduced from 16.6% to 14% following HYPR-LR-MC processing with the largest kernel used, while the average bias rises from 1.2% to 3.73% . HYPR-LR-FC processing reduces noise more dramatically, but at the cost of introduced bias [Fig. 4(b)]. The tradeoff between bias and noise is closely related to kernel size for HYPR-LR-FC. When a $3 \times 3 \times 3$ mm³ kernel is used, the average COV is reduced to 8.7% and average bias increases to 5.39% , and when a $9 \times 9 \times 9$ mm³ kernel is used, average COV drops to 5.37% and average bias increases to 11.4% . Simple smoothing does reduce the variance in the parametric images generated with RPM2 relatively well. Smoothing with the $3 \times 3 \times 3$ mm³ FWHM Gaussian reduces the average COV to 10.5% and creates a negative bias of -2.92% relative to the baseline of 1.2% .

HYPR-LR can be used alongside simple smoothing to provide even greater noise reduction without any additional

loss of spatial resolution. For example, smoothing with a $3 \times 3 \times 3$ mm³ FWHM Gaussian followed by HYPR-LR-MC processing using a $9 \times 9 \times 9$ mm³ Gaussian kernel reduces the average COV in the Logan parametric images to 7.19% , albeit while increasing bias to -6.98% , and reduces the variance in the RPM2 parametric images to 8.55% with a bias of -1.03% .

IV.B. Evaluation of human [¹¹C]-PIB data

An illustrative example of parametric images generated from a human PIB dataset with both the reference region Logan method (Fig. 5 top row) and RPM2 (Fig. 5 bottom row) qualitatively demonstrates the relative tradeoff between noise and (in the case of the Logan method) bias reduction, and introduced bias from HYPR-LR processing or simple spatial smoothing. These images are consistent with the data presented from the numerical simulations. HYPR-LR-MC reduces the variance in both the Logan and RPM2 parametric images, though the variance reduction is notably greater for the Logan images. HYPR-LR-MC processing also globally increases the BP_{ND} values in the Logan images, indicating a reduction of the noise-dependent bias. HYPR-LR-FC provides the greatest reduction in variance for both the reference Logan method and RPM2 in exchange for a slight inappropriate enhancement of the contrast between white matter and the cortex. HYPR-LR-FC likewise reduces the noise-dependent Logan bias. Smoothing with a $3 \times 3 \times 3$ mm³ FWHM Gaussian results in some improvement of the variance and bias of the Logan image, and qualitatively improves the variance in the RPM2 image to a similar degree as HYPR-LR-MC processing at the cost of some blurring. HYPR-LR processing can be done in addition to simple

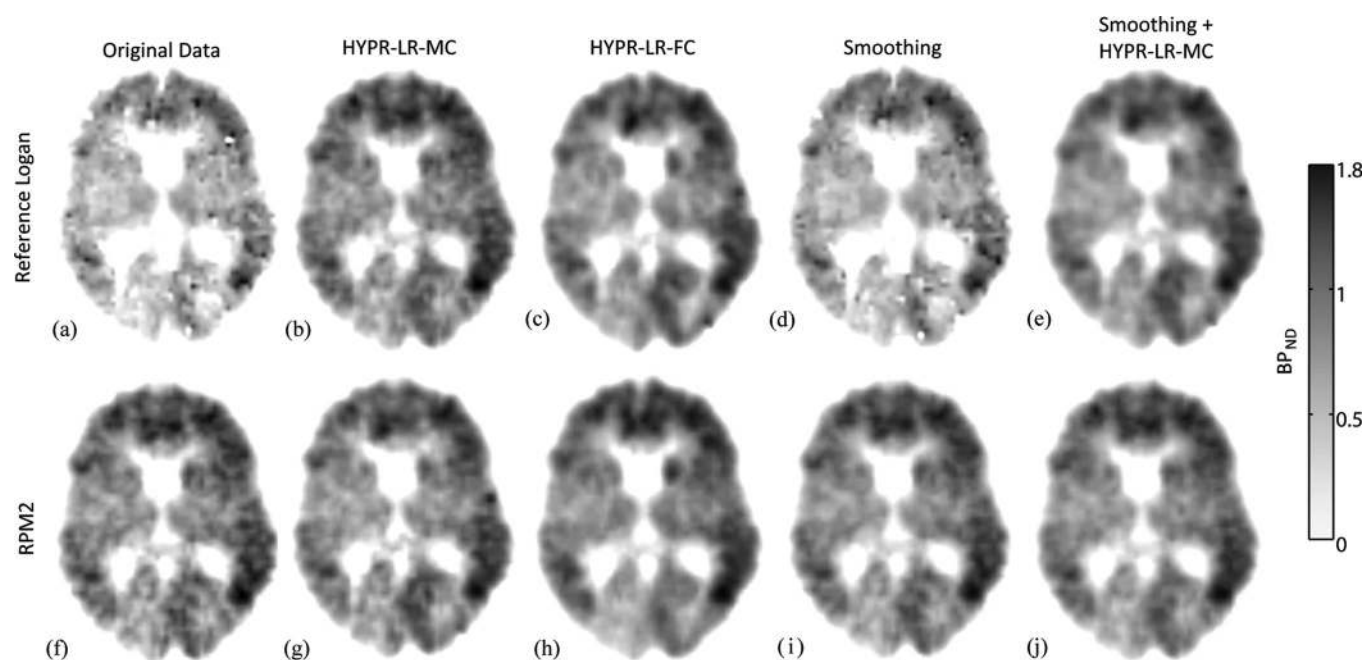


FIG. 5. An illustrative example of the effects of HYPR-LR processing on parametric images generated from a human [^{11}C]-PIB data set. The unprocessed data are predictably noisy and the Logan image (a) appears biased compared to the RPM2 image (f). HYPR-LR processing with a 9 mm FWHM Gaussian kernel improves the variance of both Logan and RPM2 parametric images (b), (c), (g), and (h). HYPR-LR-MC processing results in parametric images that have more variance, (b) and (g), than when all the frames of the study are used to form the composite, (c) and (h), but they are also likely less biased. Spatial smoothing with a $3 \times 3 \times 3 \text{ mm}^3$ Gaussian results in improved variance with a corresponding loss of spatial resolution, (d) and (i). HYPR-LR processing can also be done following smoothing to provide a further improvement in variance without any additional loss of spatial resolution, demonstrated here with HYPR-LR-MC, (e) and (j).

smoothing to further reduce variance. This is demonstrated in Fig. 5 with HYPR-LR-MC.

To evaluate bias in the real data, the average BP_{ND} values of voxels in ROIs drawn on the frontal and parietal cortices of eight parametric images were compared with the standard BP_{ND} values of TACs obtained from the same ROIs using the reference Logan method. The results from the reference Logan parametric images show that HYPR-LR-FC and HYPR-LR-MC reduce both the bias and variance of the parametric image derived BP_{ND} values as the slopes of the linear fits approach unity and all the data points fall closely around their respective fits (Fig. 6). Simple smoothing also reduces some of the noise-dependent Logan bias, but much less than the HYPR-LR processing methods. The results from the RPM2 parametric images largely reflect what is seen in the simulated data. There appears to be little bias in the RPM2 images of the original data and the HYPR-LR-MC processed data. HYPR-LR-FC does introduce a positive bias, seen in the increased BP_{ND} values and the increase of the slope of the fit from 0.97 to 1.1. Smoothing does not bias the slope of the fit, but it does reduce the y-intercept of the fit from 0.063 to 0.028, and all of the smoothed BP_{ND} values fall slightly below the original values.

Finally, we attempted to further study variance in the real data by plotting voxel values from Logan and RPM2 parametric images against each other. Assuming that noise in time-series data generates variance in the parametric images that does not perfectly co-vary between the Logan and RPM2 methods, the correlation between the BP_{ND} values obtained with the two methods should provide an

indication of variance. We do this here using the Pearson correlation coefficient. An illustrative example of voxels in the parietal and frontal cortex of the same data set shown in Fig. 5 indicates that HYPR-LR does provide a substantial increase in the correlation between BP_{ND} values derived from the different analysis methods (Fig. 7). When the correlation coefficients of all the [^{11}C]-PIB datasets are compared following smoothing and HYPR-LR processing using paired t-tests, all of the denoising methods significantly increase the correlation between BP_{ND} values obtained with Logan analysis and RPM2 ($p < 0.01$) (Table II). There is not a significant difference in the correlation coefficients between HYPR-LR-MC and HYPR-LR-FC ($p > 0.05$), but HYPR-LR-MC and HYPR-LR-FC both significantly increase the correlation over smoothing with a $3 \times 3 \times 3 \text{ mm}^3$ Gaussian. Examination of the parametric images (Fig. 5) indicates that the lower correlation coefficients of the smoothed data are due mostly to the higher noise in the Logan parametric images.

V. DISCUSSION

HYPR-LR is a promising denoising technique for PET, and here we have attempted to illustrate its ability to improve the variance and bias of parametric images derived from kinetic analysis techniques. In order to maximize the improvement in variance and bias while minimizing the error introduced by HYPR-LR processing, we have proposed a method of forming multiple, time dependent, composite images (HYPR-LR-MC) that minimizes the difference of the

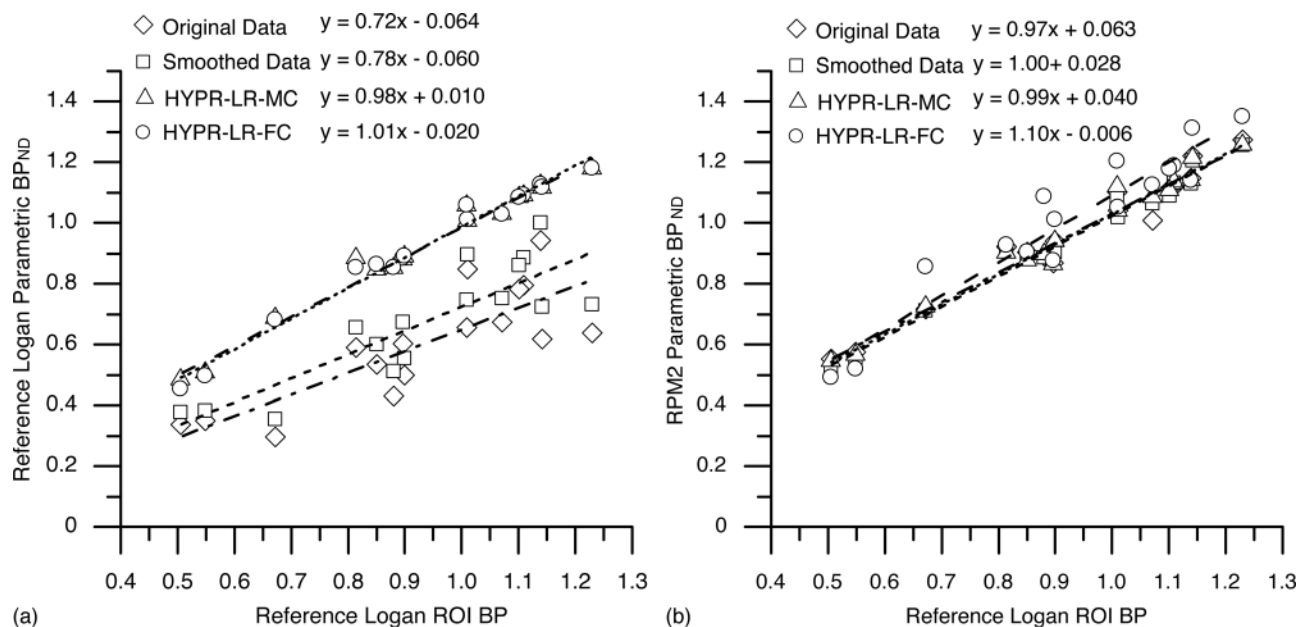


FIG. 6. BP_{ND} values obtained from ROIs drawn on the parametric Logan (a) and RPM2 (b) images compared with the BP_{ND} values obtained from the TACs of the same ROIs with the reference region Logan graphical method. Each point on the graphs represents the BP_{ND} from either the frontal or parietal cortex of one of the eight [¹¹C]-PIB positive scans studied. Linear fits to the BP_{ND} values obtained using different types of processing are also shown with their corresponding equations (--- = original data, --- = smoothed, = HYPR-LR-MC, --- = HYPR-LR-FC). A deviation of the slope from unity or a y intercept other than zero indicates the presence of a bias.

contrast between objects in each frame of the study and the frame's respective composite image. Such an approach will provide less of an improvement in noise and introduce less bias than using all the frames in the study to form the composite image. It is also less arbitrary than the traditional approach of using a sliding composite window.¹

Bias introduced by HYPR-LR processing will be dependent on differences in contrast that do exist between frames of interest and their respective composites. In the case of the simulated and human [¹¹C]-PIB presented here, HYPR-LR-FC processing distorts TACs [Fig. 3(g)] and thus inappropriately increases the BP_{ND} values obtained with both Logan graphical analysis and RPM2 in regions of high uptake where they border regions of lower uptake, and decreases the BP_{ND} values of the surrounding voxels (Fig. 3). This bias can also be seen in the overestimated BP_{ND} values of the frontal and parietal cortices in the parametric images

generated from the noisy simulated data processed with HYPR-LR-FC (Fig. 4), and in the BP_{ND} values of these same regions in the parametric images of the human datasets (Fig. 6). HYPR-LR-MC processing virtually eliminates the bias caused by HYPR-LR (Fig. 3), as it almost completely removes the noise-dependent Logan bias without overestimating BP_{ND} values, and introduces little bias into parameters obtained with RPM2 (Figs. 4 and 6). Bias can also be limited with HYPR-LR-FC if a smaller kernel size is used. In this work, the smallest kernel used was a Gaussian with a FWHM of $3 \times 3 \times 3$ mm³, only slightly larger than the thickness of the cerebral cortex, our primary object of interest. For the simulated data studied here, HYPR-LR-FC with this size kernel performed particularly well when the data were analyzed with RPM2, only introducing slightly more bias than HYPR-LR-MC with a large 9 mm FWHM filtering kernel (5.39% versus 3.73%). HYPR-LR-FC with the smaller

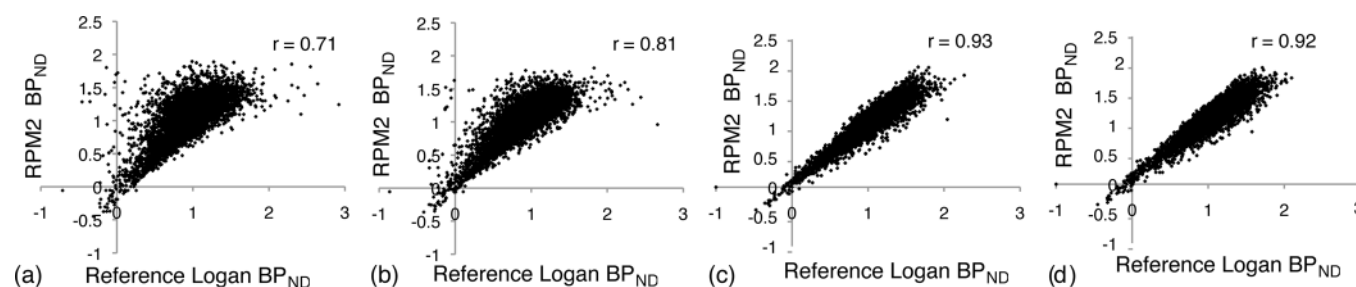


FIG. 7. Voxel BP_{ND} values obtained with the Logan graphical method and RPM2 plotted against each other from a representative [¹¹C]-PIB study. The parametric images generated from the original data (a) are compared with those generated from the data smoothed with a $3 \times 3 \times 3$ mm³ FWHM Gaussian (b), HYPR-LR-MC (c), and HYPR-LR-FC (d). The correlation between the two analysis methods, measured here with the Pearson correlation coefficient (r), gives an indication of the variance present in the parametric images.

TABLE II. The mean and range of Pearson correlation coefficients obtained from a linear fit to the voxel-by-voxel comparisons of the reference region Logan method and RPM2 for each of the eight human [^{11}C]-PIB datasets studied. The mean correlation coefficient was significantly improved with each of the denoising methods over the original data ($*p < 0.01$). There was no difference between the two implementations of HYPR-LR ($p > 0.05$), but they both increased the mean correlation coefficient more than simple smoothing ($^{+}p < 0.01$).

	Original data	Smoothed	HYPR-LR-MC	HYPR-LR-FC
Mean Pearson-r (range)	0.62 (0.42–0.88)	0.71* (0.51–0.82)	0.94* ⁺ (0.91–0.98)	0.93* ⁺ (0.89–0.98)

kernel size did not provide as much of a benefit to the data analyzed with the Logan graphical method, as BP_{ND} values are still relatively biased (Fig. 4).

Both methods of implementing HYPR-LR demonstrate an ability to reduce variance in the parametric images presented here. HYPR-LR-FC processing with a larger filtering kernel in particular substantially reduces the variance in parametric images generated with both the Logan graphical method and RPM2 (Figs. 4, 5, and 7). This is not surprising, as each individual frame in a study is given the noise properties of the fully summed composite image. Processing with our proposed HYPR-LR-MC method reduces variance more substantially in parametric images generated with the Logan graphical method (Figs. 4, 5, and 7). HYPR-LR-MC also reduces variance in the parametric images created with RPM2, but more moderately, particularly in the simulated data (Fig. 4). The results from the real data are more promising and show that HYPR-LR-MC processing visually reduces the variance seen in the example parametric image (Fig. 5), and increases the correlation between BP_{ND} values obtained with the reference Logan method and RPM2 (Fig. 7 and Table II). As expected, a larger kernel size results in better variance reduction with the HYPR-LR-MC algorithm while introducing little or no additional bias. A larger kernel likewise improves the variance reduction with the HYPR-LR-FC algorithm, but more bias is introduced as a result (Fig. 4). Using HYPR-LR-FC with a small filtering kernel may therefore be desirable in some applications. For example, when the simulated data are analyzed with RPM2, HYPR-LR-FC with a smaller kernel still achieves good variance reduction (from 16.6% to 8.7%) while introducing little bias, as discussed above.

In this work, we have compared HYPR-LR processing to simple spatial smoothing. While many other denoising methods have been developed, spatial smoothing, either within image reconstruction or afterward, remains one of the most common ways to control noise in PET data. In addition, the processing time required for HYPR-LR will not be substantially longer than the time required to spatially smooth each frame, as processing time will largely be determined by the number of convolution operations that must be performed. In this work, the number of convolutions required for HYPR-LR-MC processing is 1.6 times greater than spatially smoothing each frame. HYPR-LR processing compares very favorably to smoothing when the data are analyzed with the reference Logan graphical method. HYPR-LR-MC and HYPR-LR-FC control both bias and variance very well, whereas smoothing with the $3 \times 3 \times 3 \text{ mm}^3$ FWHM Gaussian only slightly improves the bias and variance, and

smoothing with the $6 \times 6 \times 6 \text{ mm}^3$ Gaussian controls variance very well but introduces a substantial bias of its own because of excessive blurring (Figs. 4–6). The improvements offered by HYPR-LR are less dramatic compared to simple smoothing when parametric images are created with RPM2. In the simulated data, smoothing with a $3 \times 3 \times 3 \text{ mm}^3$ FWHM Gaussian improves variance more than HYPR-LR-MC (10.5% versus 14.0%), though the smoothed BP_{ND} values are more biased relative to the unprocessed data as there is a loss of spatial resolution (Fig. 4). HYPR-LR-FC using a $3 \times 3 \times 3 \text{ mm}^3$ Gaussian kernel does provide more variance reduction than simply smoothing with a $3 \times 3 \times 3 \text{ mm}^3$ Gaussian (8.7% versus 10.5%) for a comparable amount of bias relative to the original data (Fig. 4), although the bias caused by HYPR-LR-FC is not due to any loss of spatial resolution. The human data are consistent with this, demonstrating that simple smoothing with a $3 \times 3 \times 3 \text{ mm}^3$ FWHM Gaussian reduces the variance in the RPM2 images to a greater degree than HYPR-LR-MC while only modestly blurring the data (Figs. 5 and 6). The lower correlation between the RPM2 and Logan BP_{ND} values following smoothing with the $3 \times 3 \times 3 \text{ mm}^3$ FWHM Gaussian is due to the high variance in the Logan images (Fig. 7). HYPR-LR processing can also be done in addition to simple smoothing to provide further reductions in variance in the parametric images without introducing any additional loss of spatial resolution (Figs. 4 and 5).

In the future, HYPR-LR denoising must be considered more fully in the context of other denoising methods, for example wavelet denoising and iterative image reconstruction algorithms, including the numerous proposed approaches to four-dimensional PET reconstruction, which have previously been explored as a means of improving kinetic analysis and parametric image generation.^{19–25} As HYPR-LR uses temporally integrated data to reduce noise, comparing it to denoising methods that likewise utilize the time domain, such as 4D reconstructions, will be particularly important. Iterative reconstructions, wavelet denoising, and HYPR-LR have all demonstrated an ability to substantially reduce noise, but each also has drawbacks. A full comparison between HYPR-LR and these other denoising processes, explicitly examining the pros and cons of each, is beyond the scope of the current study and will likely depend on the specific imaging task. Furthermore, as demonstrated here with spatial smoothing, as a post processing technique that is fast and relatively simple to implement, HYPR-LR could easily complement these other denoising techniques. This is particularly relevant for performing HYPR-LR on OSEM reconstructions, which are now routinely done on both

clinical and research scanners and provide some noise control themselves.

In this work, we have shown that following HYPR-LR processing, Logan and RPM2 analysis perform quite comparably. After denoising the simulated data with HYPR-LR-MC and HYPR-LR-FC processing with larger filtering kernels, both the coefficient of variation and the bias are similar between the Logan method and RPM2 (Fig. 4). If anything, after HYPR-LR processing the greater bias is seen with RPM2 with little additional benefit in variance reduction. The human data confirm this, showing little bias in the BP_{ND} values obtained with either Logan analysis or RPM2 after HYPR-LR-MC processing, and greater bias in the RPM2 data following HYPR-LR-FC processing (Fig. 6). The level of variance in the parametric images generated from the human data with the two analysis methods is also comparable following HYPR-LR processing (Figs. 5 and 7).

In addition, we found the performance of RPM2 to be more variable and sensitive to user selected parameters. In particular, we selected a minimum k_2 slightly greater than that predicted by some of the non-linear SRTM fits to the ROI TACs, and greater than the value previously reported for [^{11}C]-PIB analysis.⁹ We also see a slight positive bias in the BP_{ND} values obtained with RPM2 in the simulations (Fig. 4). This might be because the assumption of a simplified reference tissue model does not adequately describe the kinetics of [^{11}C]-PIB in this case.⁵

While our objective here is not to determine the best way to analyze [^{11}C]-PIB data, the increased reliability and greater robustness seen with Logan analysis following HYPR-LR processing may prove valuable. The Logan method is easy to implement, does not assume any particular model, and does not require imposing limits on the data, for example the range of k_2 in RPM2. HYPR-LR processing does also improve the parametric images created with RPM2, albeit not as dramatically relative to simple smoothing.

Presumably, HYPR-LR processing should also improve other data driven methods, such as the multi-linear regression methods that are not susceptible to a noise-sensitive bias but do exhibit greater variance than the Logan graphical method.^{26,27} Likewise, it should improve other model based methods like compartmental analysis.

The results presented here demonstrate that both the proposed method for forming multiple time dependent composites and simply using all the frames in the composite formation may have value in different contexts. HYPR-LR-MC introduces minimal bias but the bias introduced by HYPR-LR-FC is not that great in the data studied here, particularly when a smaller filtering kernel is used. And while HYPR-LR-MC certainly reduces variance, HYPR-LR-FC does so to a greater degree. When the focus is on relatively large regions of high uptake in [^{11}C]-PIB data, HYPR-LR-FC appears to perform relatively well. However, we still urge caution in using all frames of the study for forming the composite image. In the case of [^{11}C]-PIB, it appears as if the bias caused by HYPR-LR-FC results in greater contrast between structures in the brain. While such an image may be appealing to look at, it may be a misleading result. Bias

caused by HYPR-LR will also likely be greater in studies that have greater contrast between areas of interest and their surrounding background, for example [^{11}C]-raclopride or any of a number of tracers used to study tumor biology. It is clear that using HYPR-LR with composite images that have been formed in a way that accounts for the kinetic behavior of the tracer being studied can certainly provide an improvement in the variance of kinetic parameters while introducing very little bias.

While we have focused on the application of HYPR-LR processing to [^{11}C]-PIB data, a tracer of interest in the neuroscience community, the approach that we have presented here should be generalizable to other tracers and other applications outside the brain. Indeed, the fairly detailed structure of the brain, and of the cortex in particular, provides a good means of testing HYPR-LR processing. HYPR-LR processing may prove particularly valuable for providing more detailed physiologic information on a smaller anatomical scale for cardiac and oncology applications of dynamic PET imaging. Not all tracers will follow the exact uptake pattern we have described, and the optimal composite scheme, including simply using a fully summed composite, will depend on the application. Nevertheless, examining the ratio of the activities of neighboring regions over time will still provide valuable insight as to how HYPR-LR can be applied to maximize variance reduction while minimizing introduced bias.

VI. CONCLUSION

HYPR-LR is a promising denoising technique for a number of medical imaging modalities, and we have previously demonstrated its potential for denoising dynamic PET data. In this work, we have shown that HYPR-LR processing can improve kinetic analysis techniques used for processing dynamic PET data, and we have introduced a method for forming multiple time-dependent composite images that minimizes the bias the HYPR-LR algorithm causes while maximizing the improvement in variance it provides. This implementation of HYPR-LR could thus improve the kinetic analysis of dynamic PET data without sacrificing accuracy. In addition, our comparison between Logan graphical analysis and RPM2 before and after HYPR-LR processing provides a framework for testing the validity of HYPR-LR processing in the context of a given tracer and two methods of analysis. We envision HYPR-LR being particularly valuable in PET applications that suffer from high noise, such as PET scans requiring high spatial or temporal resolution, vulnerable patient populations who require less radiation dose, tracers used to screen large populations, and tracers utilizing unique but dosimetry limited radionuclides such as ^{124}I and ^{64}Cu . HYPR-LR is a simple denoising tool, and our proposed method for its quantitatively accurate implementation could easily be implemented for different tracer behaviors, or for individual studies.

ACKNOWLEDGMENTS

The authors would like to thank Dr. Sterling Johnson of the University of Wisconsin-Madison for providing the

human [^{11}C]-PIB data, the UW Cyclotron group for the production of the [^{11}C]-PIB, Dustin Wooten and Ansel Hilmer for assisting in the acquisition of the human data, and Kevin Cheng from Washington University, St. Louis for the helpful discussions. The authors would also like to acknowledge financial support from the University of Wisconsin Medical Scientist Training Program, the University of Wisconsin Department of Radiology, and the NIH Radiological Sciences Training Grant No. T32 CA009206.

^{a)} Author to whom correspondence should be addressed. Electronic mail: jfloberg@wisc.edu

- ¹C. A. Mistretta, O. Wieben, J. Velikina, W. Block, J. Perry, Y. Wu, K. Johnson, and Y. Wu, "Highly constrained backprojection for time-resolved MRI," *Magn. Reson. Med.* **55**, 30–40 (2006).
- ²K. M. Johnson, J. Velikina, Y. Wu, S. Kecskemeti, O. Wieben, and C. A. Mistretta, "Improved waveform fidelity using local HYPR reconstruction (HYPR LR)," *Magn. Reson. Med.* **59**, 456–462 (2008).
- ³Y. Wu, F. R. Korosec, C. A. Mistretta, and O. Wieben, "CE-MRA of the lower extremities using HYPR stack-of-stars," *J. Magn. Reson. Imaging* **29**, 917–923 (2009).
- ⁴B. T. Christian, N. T. Vandehey, J. M. Floberg, and C. A. Mistretta, "Dynamic PET denoising with HYPR processing," *J. Nucl. Med.* **51**, 1147–1154 (2010).
- ⁵J. C. Price, W. E. Klunk, B. J. Lopresti, X. Lu, J. A. Hoge, S. K. Ziolko, D. P. Holt, C. C. Meltzer, S. T. DeKosky, and C. A. Mathis, "Kinetic modeling of amyloid binding in humans using PET imaging and Pittsburgh Compound-B," *J. Cereb. Blood Flow Metab.* **25**, 1528–1547 (2005).
- ⁶J. Logan, J. S. Fowler, N. D. Volkow, A. P. Wolf, S. L. Dewey, D. J. Schlyer, R. R. MacGregor, R. Hitzemann, B. Bendriem, and S. J. Gatley, "Graphical analysis of reversible radioligand binding from time-activity measurements applied to [N-11C-methyl]-(-)-cocaine PET studies in human subjects," *J. Cereb. Blood Flow Metab.* **10**, 740–747 (1990).
- ⁷J. Logan, J. S. Fowler, N. D. Volkow, G. J. Wang, Y. S. Ding, and D. L. Alexoff, "Distribution volume ratios without blood sampling from graphical analysis of PET data," *J. Cereb. Blood Flow Metab.* **16**, 834–840 (1996).
- ⁸M. Slifstein and M. Laruelle, "Effects of statistical noise on graphic analysis of PET neuroreceptor studies," *J. Nucl. Med.* **41**, 2083–2088 (2000).
- ⁹M. Yaqub, N. Tolboom, R. Boellaard, B. N. van Berckel, E. W. van Tilburg, G. Luurtsema, P. Scheltens, and A. A. Lammertsma, "Simplified parametric methods for [^{11}C]PIB studies," *Neuroimage* **42**, 76–86 (2008).
- ¹⁰A. A. Lammertsma and S. P. Hume, "Simplified reference tissue model for PET receptor studies," *Neuroimage* **4**, 153–158 (1996).
- ¹¹R. N. Gunn, A. A. Lammertsma, S. P. Hume, and V. J. Cunningham, "Parametric imaging of ligand-receptor binding in PET using a simplified reference region model," *Neuroimage* **6**, 279–287 (1997).
- ¹²Y. Wu and R. E. Carson, "Noise reduction in the simplified reference tissue model for neuroreceptor functional imaging," *J. Cereb. Blood Flow Metab.* **22**, 1440–1452 (2002).
- ¹³C. S. Patlak, R. G. Blasberg, and J. D. Fenstermacher, "Graphical evaluation of blood-to-brain transfer constants from multiple-time uptake data," *J. Cereb. Blood Flow Metab.* **3**, 1–7 (1983).
- ¹⁴C. S. Patlak and R. G. Blasberg, "Graphical evaluation of blood-to-brain transfer constants from multiple-time uptake data. Generalizations," *J. Cereb. Blood Flow Metab.* **5**, 584–590 (1985).
- ¹⁵I. G. Zubal, C. R. Harrell, E. O. Smith, Z. Rattner, G. Gindi, and P. B. Hoffer, "Computerized three-dimensional segmented human anatomy," *Med. Phys.* **21**, 299–302 (1994).
- ¹⁶G. Brix, J. Zaers, L. E. Adam, M. E. Bellemann, H. Ostertag, H. Trojan, U. Haberkorn, J. Doll, F. Oberdorfer, and W. J. Lorenz, "Performance evaluation of a whole-body PET scanner using the NEMA protocol. National Electrical Manufacturers Association," *J. Nucl. Med.* **38**, 1614–1623 (1997).
- ¹⁷H. Herzog, L. Tellman, U. Pietrzyk, M. E. Casey, and T. Kuwert, "NEMA NU2-2001 guided performance evaluation of four siemens ECAT PET scanners," *IEEE Trans. Nucl. Sci.* **51**, 2662–2669 (2004).
- ¹⁸B. J. Lopresti, W. E. Klunk, C. A. Mathis, J. A. Hoge, S. K. Ziolko, X. Lu, C. C. Meltzer, K. Schimmel, N. D. Tsopelas, S. T. DeKosky, and J. C. Price, "Simplified quantification of Pittsburgh compound B amyloid imaging PET studies: A comparative analysis," *J. Nucl. Med.* **46**, 1959–1972 (2005).
- ¹⁹F. E. Turkheimer, M. Brett, D. Visvikis, and V. J. Cunningham, "Multiresolution analysis of emission tomography images in the wavelet domain," *J. Cereb. Blood Flow Metab.* **19**, 1189–1208 (1999).
- ²⁰F. E. Turkheimer, R. B. Banati, D. Visvikis, J. A. Aston, R. N. Gunn, and V. J. Cunningham, "Modeling dynamic PET-SPECT studies in the wavelet domain," *J. Cereb. Blood Flow Metab.* **20**, 879–893 (2000).
- ²¹J. W. Lin, A. F. Laine, and S. R. Bergmann, "Improving PET-based physiological quantification through methods of wavelet denoising," *IEEE Trans. Biomed. Eng.* **48**, 202–212 (2001).
- ²²Z. Cselenyi, H. Olsson, L. Farde, and B. Gulyas, "Wavelet-aided parametric mapping of cerebral dopamine D2 receptors using the high affinity PET radioligand [^{11}C]FLB 457," *Neuroimage* **17**, 47–60 (2002).
- ²³F. E. Turkheimer, J. A. Aston, R. B. Banati, C. Riddell, and V. J. Cunningham, "A linear wavelet filter for parametric imaging with dynamic PET," *IEEE Trans. Med. Imaging* **22**, 289–301 (2003).
- ²⁴N. M. Alpert, A. Reilhac, T. C. Chio, and I. Selesnick, "Optimization of dynamic measurement of receptor kinetics by wavelet denoising," *Neuroimage* **30**, 444–451 (2006).
- ²⁵A. Rahmim, J. Tang, and H. Zaidi, "Four-dimensional (4D) image reconstruction strategies in dynamic PET: Beyond conventional independent frame reconstruction," *Med. Phys.* **36**, 3654–3670 (2009).
- ²⁶M. Ichise, H. Toyama, R. B. Innis, and R. E. Carson, "Strategies to improve neuroreceptor parameter estimation by linear regression analysis," *J. Cereb. Blood Flow Metab.* **22**, 1271–1281 (2002).
- ²⁷J. Logan, "A review of graphical methods for tracer studies and strategies to reduce bias," *Nucl. Med. Biol.* **30**, 833–844 (2003).